Universal Return to Isotropy of Inhomogeneous Atmospheric Boundary Layer Turbulence

Ivana Stiperski[*]
Department of Atmospheric and Cryospheric Sciences, University of Innsbruck, Innsbruck 6020, Austria

Gabriel G. Katul[†]
Nicholas School of the Environment and the Department of Civil and Environmental Engineering, Duke University, Durham, North Carolina 27708, USA

Marc Calaf[‡]
Department of Mechanical Engineering, University of Utah, Salt Lake City, Utah 84112, USA

(Received 31 July 2020; revised 18 December 2020; accepted 24 March 2021; published 10 May 2021)

A recalcitrant problem in the physics of turbulence is the representation of the tendency of large-scale anisotropic eddies to redistribute their energy content with decreasing scales, a phenomenon referred to as return to isotropy. An unprecedented dataset of atmospheric turbulence measurements covering flat to mountainous terrain, stratification spanning convective to very stable conditions, surface roughness ranging over several orders of magnitude, and Reynolds numbers that far exceed the limits of direct numerical simulations and laboratory experiments was assembled for the first time and used to explore the scalewise return to isotropy. The multiple routes to energy equipartitioning among velocity components are shown to be universal once the initial anisotropy at large scales, linked to turbulence generation, is accounted for.

DOI: 10.1103/PhysRevLett.126.194501

One of the universal characteristics of all turbulent flows is the tendency to return to isotropy at small scales. In inhomogeneous flows, this tendency is forced by the lack of equipartitioning of turbulence kinetic energy (TKE) among the three velocity components at large scales. The return to isotropy is the outcome of one of the least understood mechanisms in the Navier-Stokes equations: the interaction between the turbulent pressure and velocity gradients (i.e., pressure-strain interaction). In 1951, Rotta proposed the now celebrated model that assumes a linear relation between the degree of anisotropy (of large eddies) and the rate at which the flow returns to an equipartitioned energy state through the energy cascade [1], nowadays broadly accepted in all turbulence modeling, be it for engineering or geophysical applications [2], including numerical weather predictions [3]. This work, marking a major departure from the eddy viscosity theories of Boussinesq [4] and the mixing length hypothesis of Prandtl [5], considered a statistical equilibrium of TKE and its components for the first time. Atmospheric surface layer (ASL) flows are a quintessential example of high Reynolds number turbulence that is anisotropic in eddy sizes, the distribution of TKE among its three velocity components and finite stresses. The anisotropy is sustained by multiple mechanisms that include injection (or removal) of energy along a given velocity component (shear in the horizontal, buoyancy in the vertical), and external distortions due to advection and mean pressure gradients encountered in flow over topography. Formulating the route taken to achieve energy redistribution among velocity components as the energy cascade progresses down scale (i.e., tendency to return to isotropy) remains a formidable challenge. An unprecedented ensemble of ASL turbulence measurements is assembled here for the first time to explore the scalewise route of return to isotropy for atmospheric turbulence at the crossover from large to inertial scales. The datasets differ vastly in terrain type (flat to mountainous), measurement heights (near vegetation top to above ASL), surface roughness, and thermal stratification (convective to strongly stably stratified), thus representing an exhaustive range of real-world conditions (datasets and post-processing methods are described in Supplemental Material, Sec. A [6]). The results demonstrate that for a given anisotropic state at scales larger than the integral length scale, turbulent eddies follow a universal route when relaxing towards an approximate equipartition of energy at smaller scales, and that this route is independent of external sources of heterogeneity affecting the flow. This finding is remarkable when considering the associated degrees of freedom in the energy cascade exceeding

10^{15}, the extensive range of surface roughnesses and thermal stratifications, as well as cases where terrain-induced mean pressure gradients and flow distortions by mean advection and flow separation significantly affect the TKE budget.

Return to isotropy trajectories across scales.—For any statistical state of turbulence it is possible to construct a Reynolds stress tensor defined by its components $\overline{u_i'u_j'}$, where the turbulent velocity component u_i' acting along direction x_i ($i = 1, 2, 3$ being longitudinal, lateral, and surface normal) is defined as an excursion from the time-averaged state $\overline{u_i}$, and the coordinate axes are transformed so that $\overline{u_2} = \overline{u_3} = 0$. The trace of $\overline{u_i'u_j'}$ is twice the TKE ($k = 0.5\overline{u_l'u_l'}$), indicating turbulence intensity, while the off-diagonal terms (i.e., turbulent shear stresses) are responsible for transporting momentum [21]. According to Lumley and Newman [22], a state in which all stresses are zero and k is equipartitioned between the three velocity components is labeled as isotropic at a point.

The degree of anisotropy at a point can be characterized by two anisotropy invariants (ξ, η) [21,22]:

$$\eta^2 = \frac{1}{3}(\lambda_1^2 + \lambda_1\lambda_2 + \lambda_2^2); \qquad \xi^3 = -\frac{1}{2}\lambda_1\lambda_2(\lambda_1 + \lambda_2), \tag{1}$$

where λ_1, λ_2, λ_3 are the three eigenvalues of the anisotropy stress tensor defined by its components $b_{ij} = (\overline{u_i'u_j'}/\overline{u_l'u_l'}) - (1/3)\delta_{ij}$. This representation of anisotropy allows a unique mapping of any realizable state of turbulence onto a two-dimensional nonlinear map spanned by the two invariants, the so-called anisotropy invariant map (AIM). The highly distorted nature of AIM, however, impedes clear interpretation of the trajectories within it, thus, we choose a transformation onto an alternative set of invariants (x_B, y_B) [23] defined as

$$x_B = \lambda_1 - \lambda_2 + \frac{1}{2}(3\lambda_3 + 1); \qquad y_B = \frac{\sqrt{3}}{2}(3\lambda_3 + 1), \tag{2}$$

as it yields a linear representation of anisotropy on an equilateral triangle called the barycentric map (BAM, Fig. 1). A unique mapping between the different sets of invariants ensures that our choice does not affect the key findings here. Based on the corresponding contribution of each of the eigenvalues, the topological structure of turbulence can be classified into three limiting states found at the vertices of the triangle (Fig. 1): one-component (one eigenvalue larger than zero), two-component axisymmetric (two eigenvalues larger than zero and equal), or isotropic (three eigenvalues larger than zero and equal) [21]. The in-between states found at the sides of the triangle correspond to two-component, prolate spheroid, and oblate spheroid, while the state in which at least one eigenvalue is zero

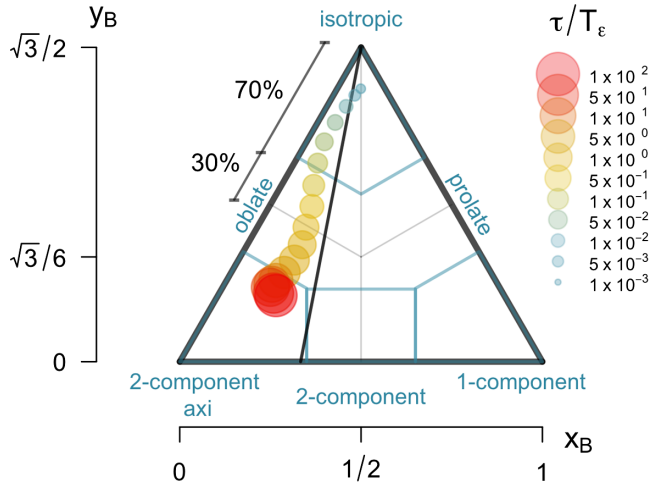

FIG. 1. Example average scalewise return-to-isotropy trajectory in barycentric coordinates for METCRAX II NEAR tower data [24] with two-component axisymmetric bulk anisotropy. Circles represent the value of nondimensional timescale τ/T_ε. The limiting states of anisotropy (blue text) and their respective ranges used for clustering (blue kites and a square emanating from the pure states) are indicated. Solid black line is the PSL.

corresponds to plane-strain limit (PSL) defined as $y_{ps} = 6(x_{ps} - 1/2) + 1$ [23].

The scalewise path turbulence takes while relaxing to isotropy constitutes a return-to-isotropy trajectory and represents a sequence of anisotropic states at decreasing scales [25,26] (Fig. 1). To obtain a trajectory for each averaging period (i.e., run), we calculate the scalewise anisotropy invariants from the cospectra of the elements of the Reynolds stress tensor, using multiresolution flux decomposition (MRD) [27]. MRD is an orthonormal decomposition based on Haar wavelet transform that decomposes the measured time series into dyadic timescales τ (see Supplemental Material, Sec. A.3 [6]). The scalewise anisotropy tensor can therefore be defined as

$$b_{ij}(\tau) = \frac{\overline{\Delta u_i'(\tau)\Delta u_j'(\tau)}}{\overline{\Delta u_l'(\tau)\Delta u_l'(\tau)}} - \frac{1}{3}\delta_{ij}, \tag{3}$$

where $\Delta u_k'(\tau) = u_k - \overline{u_k(\tau)}$ are velocity increments at scale τ. For large τ, the original anisotropy stress tensor is recovered and we refer to anisotropy at that scale as bulk anisotropy. However, at finer scales where local isotropy may be fully attained, $b_{ij}(\tau) = 0$ is not precisely congruent with isotropic turbulence theories [28], although it is also not far from them (see Supplemental Material, Sec. C [6]). Thus, $b_{ij}(\tau) \to 0$ with decreasing τ must only be viewed as a tendency to extinguish bulk anisotropy by scalewise energy redistribution as originally conceived by Rotta (thus the label return-to-isotropy is adopted here). In keeping with common turbulence models, τ was normalized using a

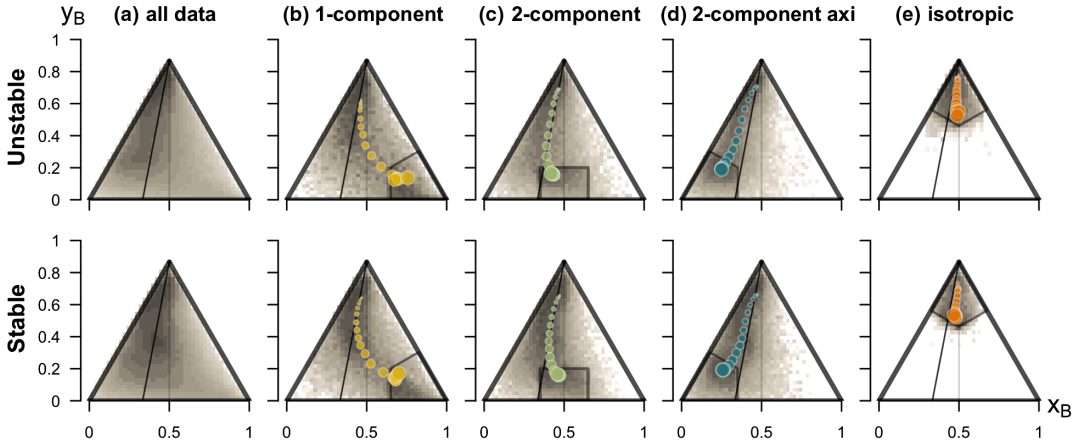

FIG. 2. Two-dimensional density plots of the scalewise anisotropy for (a) all data, and data clustered according to bulk anisotropy into (b) one-component, (c) two-component, (d) two-component axisymmetric, and (e) isotropic, for unstable (top) and stable (bottom) stratification. Colored circles show ensemble trajectories for each cluster.

dissipation time scale $T_\varepsilon = k/\varepsilon$ [21], where ε is the TKE dissipation rate (see Supplemental Material, Sec. A.2 [6]).

The trajectories obtained from each dataset were clustered based on atmospheric stratification and bulk anisotropy. The stratification was determined by the sign of the buoyancy flux and labeled as unstable (stable) for buoyancy flux directed away from (towards) the surface. The bulk anisotropy was separated into isotropic, two-component axisymmetric, two-component and one-component by imposing distance thresholds from the pure states of anisotropy (70% of half the side of BAM from each vertex) (cf. Fig. 1) as described in Ref. [29]. This clustering determines the starting point of the trajectory for each run. An ensemble trajectory for each cluster was calculated from all datasets using bin medians at logarithmically spaced nondimensional timescales τ/T_ε (cf. Figs. 1 and 2). We used random sampling with replacement in each cluster to ensure that each dataset is given equal weight in the final ensemble trajectory for that cluster despite originally having different record lengths.

Results.—According to the classical picture of linear relaxation towards isotropy [1], the return-to-isotropy trajectories are straight lines in AIM and BAM that converge towards the isotropic vertex. In contrast, trajectories in nonlinear return-to-isotropy models [30–33] are curved in ways that depend on bulk anisotropy and converge in regions of the anisotropy map that are far from the isotropic vertex. The divergence between the shapes of trajectories of different datasets can thus indicate whether relaxation to isotropy is dictated by the boundary conditions or whether their effect is fully contained in the bulk anisotropy and has minor impact on the trajectories (shapes of trajectories agree) thus implying the existence of universal pathways towards isotropy (the main conjecture here).

The cumulative two dimensional probability density plots [Fig. 2(a)] show that irrespective of stratification, ASL turbulence can attain almost all permissible states of anisotropy. The likelihood for scalewise anisotropy is highest in the upper near-isotropic part of BAM close to the oblate side, but more diffuse in the lower more anisotropic part, and especially small on the prolate side. Because of random sampling used here, the information on the anisotropy climatology for each dataset is, nonetheless, hidden. When the data are clustered according to their bulk anisotropy unique regions with highest likelihood emerge, suggesting the existence of preferential pathways towards isotropy, despite vastly different characteristics of each of the datasets. Unique ensemble trajectories [Figs. 2(b)–2(e)], representing these different pathways, are clearly determined by bulk anisotropy (i.e., anisotropy at trajectory origin) and its position relative to PSL, as previously noted by Klipp [26]. Thus one-component and two-component trajectories originating to the right of PSL follow a right-turning "boomerang-shape" path [Figs. 2(b),2(c)] converging towards and then following PSL at smaller scales. Of all the cases, the highly anisotropic one-component trajectories take the longest to reach isotropy both in terms of distance in BAM and scale. They enter the near-isotropic region in Fig. 1 only at average scales of $\tau/T_\varepsilon = 0.02$–$0.04$. Although similarly shaped, two-component trajectories [Fig. 2(c)] approach PSL sooner and reach near-isotropy already at $\tau/T_\varepsilon = 0.05$–$0.07$. Two-component axisymmetric turbulence [Fig. 2(d)] originating to the left of PSL shows an equally fast approach to near-isotropy as two-component turbulence. The trajectories, however, are almost straight (though indicating meandering for stable stratification) and run parallel to PSL, although at small scales they veer towards the oblate spheroid side of BAM. Finally, the trajectories for near-isotropic turbulence [Fig. 2(e)] follow the shortest path (i.e., straight line at the center of BAM) towards the isotropic vertex.

The spread around the ensemble trajectories (Figs. 2 and 3) indicates that individual trajectories vary both between the datasets and within each dataset, particularly

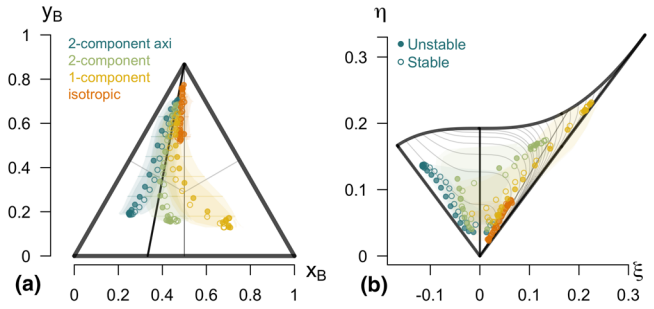

FIG. 3. Ensemble return-to-isotropy trajectories in (a) BAM and (b) AIM, for four clusters and two stratifications. Shading shows interquartile range. Black straight line is PSL, gray straight line is the line through the center of BAM, and curved gray lines are nonlinear trajectories of Ref. [30].

for one-component turbulence. Still, the shape of the trajectories in each cluster uniquely matches the shape of the corresponding ensemble trajectory, while the spread of trajectories in each cluster is contained within the spread of trajectories from flat and horizontally homogeneous terrain (see Supplemental Material, Sec. B [6]). This suggests that large disparity in surface conditions does not affect the uniqueness of identified pathways of return to isotropy.

The question still remains whether stratification, a mechanism that produces or destroys TKE via the $\overline{u_3'^2}$ budget, influences the return to isotropy in the ASL. Contrary to expectations that stratification persistently maintains anisotropy well beyond the integral length scale and that the behavior in stable and unstable stratification is asymmetric, the ensemble trajectories (Fig. 3) show a minimal variation in shape between the two stratifications, although stable trajectories show a tendency to be more curved and more attracted towards PSL. Indeed, the value of median absolute deviation (MAD) between stable and unstable trajectories for one-component (0.03), two-component (0.02) and two-component axisymmetric turbulence (0.01) is significantly smaller than MAD between the anisotropy types (0.12 between two-component axisymmetric and one-component, and 0.05 between two-component axisymmetric and two-component). Therefore, once boundary conditions acting on the flow (forcing mechanisms and stratification) set the anisotropic state of the large-scale turbulence (i.e., origin of the trajectory), the corresponding $b_{ij}(\tau)$ will follow one of the identified mean routes towards isotropy. As the equipartitioned state is approached, the return-to-isotropy mechanism becomes less efficient at energy redistribution, and conventional mechanisms describing local isotropy for two-point statistics [28] become more dominant.

Similar results are obtained for ensemble trajectories in AIM [Fig. 3(b)]. This representation allows comparing our results to known nonlinear return-to-isotropy models of homogeneous turbulence, such as the widely used model of Sarkar and Speziale [30]. All anisotropic ASL trajectories significantly depart from those of Ref. [30]. In particular, trajectories for two-component and one-component turbulence are perpendicular to those of Ref. [30], and diverge from the right prolate side of AIM where all the trajectories from Ref. [30] converge. This difference might stem from the low Reynolds number of Ref. [30] and the fact that idealized wind tunnel and DNS results in literature mostly focus on homogeneous decaying turbulence where transport and shear production are neglected in the component-wise energy and momentum-flux Reynolds-averaged budget equations. ASL datasets here do not possess such "niceties" and none of the budget terms can be *a priori* ignored. Still, some similarities to homogeneous and neutral engineering flows emerge since the exact shape of return-to-isotropy trajectories is dependent on the original state of anisotropy, indicative of a nonlinear behavior [30–33]. This nonlinearity (i.e., trajectory curvature) is a function of distance of bulk anisotropy from PSL so that trajectories initiated furthest away from PSL have largest curvature while those close to PSL are almost linear (see Supplemental Material, Sec. B [6]).

Discussion.—BAM itself suggests immanent constraints on the trajectories, thus explaining why certain trajectory shapes are favored once initial anisotropy at the largest scales is set. Because of the large scale separation characterizing the trajectories, we introduce a logarithmic dimensionless timescale $\tau_n = \log_{10}(\tau/T_\epsilon)$. Here $\tau_n \approx 1$ marks the scale where the magnitudes of the eigenvalues commence their decline with decreasing scale and at $\tau_n \to -\infty$ approach $\lambda_i(\tau_n) \to 0$. If x_B and y_B are functions of τ_n and $G(\tau_n) = \lambda_1(\tau_n) - \lambda_2(\tau_n)$, then Eq. (2) can be used to formulate trajectories in BAM and their corresponding velocities

$$\dot{x}_B(\tau_n) = \dot{G}(\tau_n) + \frac{1}{\sqrt{3}}\dot{y}_B(\tau_n), \quad \dot{y_B}(\tau_n) = \frac{3\sqrt{3}}{2}\dot{\lambda}_3(\tau_n). \tag{4}$$

Here $\dot{s}(\tau_n)$ represents $ds(\tau_n)/d\tau_n$ of any variable s. In BAM $y_B(\tau_n)$ and $\dot{y}_B(\tau_n)$ are linearly proportional to $\lambda_3(\tau_n)$ and $\dot{\lambda}_3(\tau_n)$.

Figure 4, showing the behavior of the two right-hand terms in Eqs. (2) and (4), indicates the existence of three scalewise regions loosely separated by $\tau_n \approx 1$ and $\tau_n \approx -2$. In the first region ($\tau_n > 1$), trajectories are approximately stagnant so that $\dot{G} \approx 0$ and $\dot{\lambda}_3 \approx 0$ (except for the near-isotropic cluster). Here x_B and y_B are entirely set by $G(\tau_n = 1) \approx 2/3, 1/3$ and $\lambda_3(1) = -1/3$ for one-component and two-component cases, respectively. In the second region ($-2 < \tau_n < 1$), the approach to isotropy is accompanied by the approach of $G(\tau_n), \lambda_3(\tau_n) \to 0$. The rate at which $G(\tau_n)$ decreases with decreasing scale ($\dot{G}$) is a linear function of the initial value of the largest eigenvalue $\lambda_1(\tau_n = 1)$ for all four types of trajectories, reminiscent of Rotta's linear return to isotropy but differing in the fact

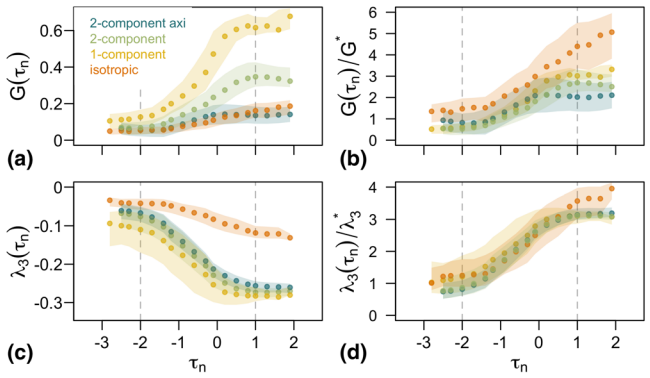

FIG. 4. Ensemble scalewise eigenvalues corresponding to trajectories in Fig. 3 for unstable stratification: (a) $G(\tau_n) = \lambda_1(\tau_n) - \lambda_2(\tau_n)$, and (c) $\lambda_3(\tau_n)$, and their scaled values normalized by (b) $G^* = 0.54\lambda_1(\tau_n = 1) - 0.04$ and (d) $\lambda_3^* = 0.35\lambda_3(\tau_n = 1) + 0.01$. The nondimensional timescale is defined as $\tau_n = \log_{10}(\tau/T_\epsilon)$.

that the linear behavior here is observed in $\log_{10}(\tau/T_\epsilon)$ and is thus exponential. This behavior can be used to provide a scaling $G^* = a\lambda_1(\tau_n = 1) + b$ that allows G/G^* trajectories to collapse in the region of their largest decrease [Fig. 4(b)]. Similarly, $\lambda_3(\tau_n)$ and $\dot{\lambda}_3(\tau_n)$ are monotonic functions [Fig. 4(c)], so that $\dot{y}_B(\tau_n) < 0$ with decreasing (and negative) τ_n leads to $y_B(\tau_n)$ monotonically increasing towards $\sqrt{3}/2$. The largest value of $\dot{\lambda}_3(\tau_n)$ is also proportional to $\lambda_3(\tau_n = 1)$ and can be scaled accordingly [Fig. 4(d)]. In the third region ($\tau_n \to -\infty$), the decrease of all trajectories slows down as they approach PSL and are forced to follow it towards isotropy. Hence, the larger the bulk anisotropy (larger λ_1), the larger and faster is the decrease of eigenvalues with decreasing scale and the convergence of trajectories towards PSL. When G is large, as for the one-component and two-component initial conditions, $|\dot{G}| > (1/\sqrt{3})|\dot{y}_B|$ and $\dot{x}_B > 0$, meaning that with negative τ_n, x_B is reduced from its initial state and trajectories move to the left explaining the boomerang path. Once the trajectories intersect PSL, deviations from it are prohibited and return to isotropy must follow PSL. For the two-component axisymmetric cases, found to the left of PSL, y_B is still monotonically approaching $\sqrt{3}/2$ but $G(\tau_n)$ is small and does not vary appreciably with scale. Hence, $\dot{x}_B$ follows $\dot{y}_B = (3/2)\dot{\lambda}_3$ (i.e., trajectories move to the right) until PSL is intersected. Again, the trajectories are general, provided $G(\tau_n)$ is small for these two regimes. Finally, for the near-isotropic cases, $x_B \approx 1/2$ and $\dot{x}_B \approx 0$ so that the variation in trajectories is contained in the y_B component driven by the finite λ_3 and the shortest distance to the upper vertex is followed. Hence, the ASL experiments attribute the universal character of return to isotropy to the collapse of data onto λ_3/λ_3^* and G/G^*. This finding is, in essence, expanding Rotta's conjecture to the scalewise evolution of eigenvalues associated with the stress tensor cospectrum.

Figures 3 and 4 also show that none of the trajectories actually attain isotropy (i.e., arrive at the isotropic vertex), rather the eigenvalues remain finite even after $\tau_n < -2$. As noted earlier and discussed further in Supplemental Material, Sec. C [6], for homogeneous decaying turbulence local isotropy does not imply equipartitioning of energy within the inertial subrange [28] since the longitudinal structure function is smaller than the lateral and wall-normal ones (i.e., ratio to the wall-normal structure function is 3/4, 1, 1 instead of 1, 1, 1). Hence, local isotropy at very fine (inertial to viscous) scales requires considerations of all aspects of the two-point statistics not fully captured by $b_{ij}(\tau)$. Besides, the limitations of sonic anemometer path length (10 cm), sampling frequency (20 Hz), and finite shear at all τ_n [34] also explain why full local isotropy (i.e., 3/4 partitioning) is not attained despite almost one decade of energy cascading.

I. S. acknowledges support from the Austrian Science Fund (FWF, Grant No. T781-N32). M. C. and G. K. acknowledge support from the U.S. National Science Foundation (NSF-PDM-1649067, NSF-PDM-1712538, NSF-AGS-1644382, NSF-AGS-2028633, and NSF-IOS-1754893). M. C. acknowledges support of the Alexander von Humboldt-Stiftung, *Humboldt Research Fellowship for Experienced Researchers*, during the sabbatical year at the Karlsruhe Institute of Technology Campus Alpin in Garmisch-Partenkirchen.

*ivana.stiperski@uibk.ac.at
†gaby@duke.edu
‡marc.calaf@utah.edu

[1] J. Rotta, Statistische Theorie nichthomogener Turbulenz, Z. Phys. **129**, 547 (1951).
[2] B. E. Launder, G. J. Reece, and W. Rodi, Progress in the development of a Reynolds-stress turbulence closure, J. Fluid Mech. **68**, 537 (1975).
[3] G. L. Mellor and T. Yamada, Development of a turbulence closure model for geophysical fluid problems, Rev. Geophys. **20**, 851 (1982).
[4] F. G. Schmitt, About Boussinesq's turbulent viscosity hypothesis: Historical remarks and a direct evaluation of its validity, C. R. Méc. **335**, 617 (2007).
[5] P. Bradshaw, Possible origin of Prandtl's mixing-length theory, Nature (London) **249**, 135 (1974).
[6] See Supplemental Material at http://link.aps.org/supplemental/10.1103/PhysRevLett.126.194501 containing information on data sets, data post-processing, trajectory calculations and inter-data set variability, which includes Refs. [7–20].
[7] S. Salesky and M. Chamecki, Random errors in turbulence measurements in the atmospheric surface layer: Implications for Monin-Obukhov similarity theory, J. Atmos. Sci. **69**, 3700 (2012).
[8] G. S. Poulos, W. Blumen, D. C. Fritts, J. K. Lundquist, J. Sun, S. P. Burns, C. Nappo, R. Banta, R. Newsom, J. Cuxart, E. Terradellas, B. Balsley, and M. Jensen,

CASES-99: A comprehensive investigation of the stable nocturnal boundary layer, Bull. Am. Meteorol. Soc. **83**, 555 (2002).

[9] V. Grubišić, J. D. Doyle, J. Kuettner, R. Dirks, S. A. Cohn, L. L. Pan, S. Mobbs, R. B. Smith, C. D. Whiteman, S. Czyzyk, S. Vosper, M. Weissmann, S. Haimov, S. F. J. D. Wekker, and F. K. Chow, The Terrain-induced Rotor Experiment, Bull. Am. Meteorol. Soc. **89**, 1513 (2008).

[10] T. Morrison, M. Calaf, C. Higgins, S. A. Drake, A. Perelet, and E. Pardyjak, The impact of surface temperature heterogeneity on near-surface heat transport, Boundary-Layer Meteorol. (to be published).

[11] A. C. M. Beljaars and F. C. Bosveld, Cabauw data for the validation of land surface parameterization schemes, J. Clim. **10**, 1172 (1997).

[12] M. W. Rotach, I. Stiperski, O. Fuhrer, B. Goger, A. Gohm, F. Obleitner, G. Rau, E. Sfyri, and J. Vergeiner, Investigating exchange processes over complex topography: The Innsbruck box (i-Box), Bull. Am. Meteorol. Soc. **98**, 787 (2017).

[13] I. Stiperski, M. Calaf, and M. W. Rotach, Scaling, anisotropy, and complexity in near-surface atmospheric turbulence, JGR Atmos. **124**, 1428 (2019).

[14] M. Chamecki and N. L. Dias, The local isotropy hypothesis and the turbulent kinetic energy dissipation rate in the atmospheric surface layer, Q. J. R. Meteorol. Soc. **130**, 2733 (2004).

[15] C. Klipp, Turbulence anisotropy in the near-surface atmosphere and the evaluation of multiple outer length scales, Bound.-Lay. Meteorol. **151**, 57 (2014).

[16] G. G. Katul, M. B. Parlange, and C. R. Chu, Intermittency, local isotropy, and non-gaussian statistics in atmospheric surface layer turbulence, Phys. Fluids **6**, 2480 (1994).

[17] M. Falocchi, L. Giovannini, M. de Franceschi, and D. Zardi, A method to determine the characteristic time-scales of quasi-isotropic surface-layer turbulence over complex terrain: A case-study in the Adige valley (Italian Alps), Q. J. R. Meteorol. Soc. **145**, 495 (2019).

[18] A. Kolmogorov, The local structure of turbulence in incompressible viscous fluid for very large Reynolds numbers, Proc. R. Soc. Lond. A **434**, 9 (1991).

[19] S. Saddoughi and S. Veeravalli, Local isotropy in turbulent boundary layers at high Reynolds number, J. Fluid Mech. **268**, 333 (1994).

[20] G. G. Katul, C. Manes, A. Porporato, E. Bou-Zeid, and M. Chamecki, Bottlenecks in turbulent kinetic energy spectra predicted from structure function inflections using the von Kármán-Howarth equation, Phys. Rev. E **92**, 033009 (2015).

[21] S. B. Pope, *Turbulent Flows* (Cambridge University Press, Cambridge, England, 2000), p. 771.

[22] J. Lumley and G. Newman, The return to isotropy of homogeneous turbulence, J. Fluid Mech. **82**, 161 (1977).

[23] S. Banerjee, R. Krahl, F. Durst, and C. Zenger, Presentation of anisotropy properties of turbulence, invariants versus eigenvalue approaches, J. Turbul. **8**, N32 (2007).

[24] M. Lehner *et al.*, The METCRAX II field experiment: A study of downslope windstorm-type flows in Arizona's Meteor Crater, Bull. Am. Meteorol. Soc. **97**, 217 (2016).

[25] P. Brugger, G. G. Katul, F. De Roo, K. Kröniger, E. Rotenberg, S. Rohatyn, and M. Mauder, Scalewise invariant analysis of the anisotropic Reynolds stress tensor for atmospheric surface layer and canopy sublayer turbulent flows, Phys. Rev. Fluids **3**, 054608 (2018).

[26] C. Klipp, Turbulence anisotropy in the atmospheric boundary layer, in *American Meteorological Society 20th Conference on Boundary Layers and Turbulence* (American Meteorological Society, Boston, 2012).

[27] J. F. Howell and L. Mahrt, Multiresolution flux decomposition, Bound.-Lay. Meteorol. **83**, 117 (1997).

[28] A. Kolmogorov, Dissipation of energy in locally isotropic turbulence, Proc. R. Soc. Lond. A **434**, 15 (1991).

[29] I. Stiperski and M. Calaf, Dependence of near-surface similarity scaling on the anisotropy of atmospheric turbulence, Q. J. R. Meteorol. Soc. **144**, 641 (2018).

[30] S. Sarkar and C. G. Speziale, A simple nonlinear model for the return to isotropy in turbulence, Phys. Fluids A **2**, 84 (1990).

[31] M. K. Chung and S. K. Kim, A nonlinear return-to-isotropy model with Reynolds number and anisotropy dependency, Phys. Fluids **7**, 1425 (1995).

[32] K.-S. Choi and J. L. Lumley, The return to isotropy of homogeneous turbulence, J. Fluid Mech. **436**, 59 (2001).

[33] H. Warrior, S. Mathews, S. Maity, and K. Sasmal, An improved model for the return to isotropy of homogeneous turbulence, J. Fluids Eng. **136**, 034501 (2014).

[34] G. G. Katul, A. Porporato, C. Manes, and C. Meneveau, Co-spectrum and mean velocity in turbulent boundary layers, Phys. Fluids **25**, 091702 (2013).